How to cite: *Angew. Chem. Int. Ed.* **2022,** *61,* e202204711
International Edition: doi.org/10.1002/anie.202204711
German Edition: doi.org/10.1002/ange.202204711

Photocatalytic Water Splitting

Atomically Dispersed Janus Nickel Sites on Red Phosphorus for Photocatalytic Overall Water Splitting

Menglong Wang, Shuai Xu, Zhaohui Zhou, Chung-Li Dong, Xu Guo, Jeng-Lung Chen, Yu-Cheng Huang, Shaohua Shen, Yubin Chen, Liejin Guo, and Clemens Burda**

Abstract: Single-atom nickel catalysts hold great promise for photocatalytic water splitting due to their plentiful active sites and cost-effectiveness. Herein, we adopt a reactive-group guided strategy to prepare atomically dispersed nickel catalysts on red phosphorus. The hydrothermal treatment of red phosphorus leads to the formation of P–H and P–OH groups, which behave as the reactive functionalities to generate the dual structure of single-atom P–Ni and P–O–Ni catalytic sites. The produced single-atom sites provide two different functions: P–Ni for water reduction and P–O–Ni for water oxidation. Benefitting from this specific Janus structure, Ni-red phosphorus shows an elevated hydrogen evolution rate compared to Ni nanoparticle-modified red phosphorus under visible-light irradiation. The hydrogen evolution rate was additionally enhanced with increased reaction temperature, reaching 91.51 $\mu mol\,h^{-1}$ at 70 °C, corresponding to an apparent quantum efficiency of 8.9 % at 420 nm excitation wavelength.

Introduction

Photocatalytic hydrogen evolution through water splitting is a promising route to fulfill the increasing energy demand and solve environmental issues.[1] Although tremendous progress has been achieved, most photocatalysts still suffer from inherent fast charge recombination and sluggish surface reactivity, leading to poor solar to hydrogen conversion efficiency.[2] Employing suitable cocatalysts is indispensable in promoting photocatalytic hydrogen evolution or oxygen evolution and further enhancing the overall efficiency for the splitting of pure water.[3] Single-atom cocatalysts have recently attracted much attention due to their numerous active sites with potentially high activity.[4] Familiar noble metal single atoms, such as Pt, Pd, and Ru, have been widely reported for various applications in photocatalytic and electrocatalytic reactions.[5] Additionally, single-atom nickel catalysts have exhibited excellent catalytic performance for water splitting and showed potential for widespread application due to the low cost involved.[6] However, the reaction mechanisms of Ni as a single-atom cocatalyst are still unclear.

Regarding the choice of the cocatalyst, the photoelectrochemical matching of cocatalysts with the main photocatalysts plays an important role in determining the photocatalytic efficiency. To effectively utilize the visible light of the solar spectrum, photocatalysts with a narrow energy gap should be developed.[7] Among them, red phosphorus (RP) has received increased attention as an elemental photocatalyst for water splitting owing to its nonmetal character, earth abundance, and broad spectral light response. Various allotropic phases of phosphorus provide tunable structures, light absorption, and optoelectronic properties to meet the requirements for photocatalytic hydrogen production. RP can be easily modified or integrated with other photoactive constituents to introduce physicochemical properties that are favorable toward photocatalysis.[8] Indeed, nickel phosphides[9] and phosphates[10] are efficient cocatalysts for water reduction and oxidation. The simultaneous existence of nickel phosphide and nickel phosphate could cooperatively enhance hydrogen and oxygen evolution.[11] Thus, it is a fascinating challenge to fabricate an advanced system for enhanced photocatalytic water splitting composed of two

[*] M. Wang, Dr. X. Guo, Prof. S. Shen, Prof. Y. Chen, Prof. L. Guo
International Research Center for Renewable Energy, State Key Laboratory of Multiphase Flow in Power Engineering,
Xi'an Jiaotong University
Shaanxi, 710049 (China)
E-mail: ybchen@mail.xjtu.edu.cn

Prof. C. Burda
Department of Chemistry, Case Western Reserve University
Cleveland, OH 44106 (USA)
E-mail: burda@case.edu

S. Xu, Prof. Z. Zhou
Chemical Engineering and Technology, School of Water and Environment, Key Laboratory of Subsurface Hydrology and Ecological Effects in Arid Region, Ministry of Education,
Chang'an University
Xi'an 710064 (China)

Prof. C.-L. Dong, Dr. Y.-C. Huang
Department of Physics, Tamkang University
New Taipei City, 25137 (Taiwan)

J.-L. Chen
National Synchrotron Radiation Research Center
Hsinchu 30076 (Taiwan)

different Ni single-atom sites on RP, utilizing the chemical interaction of the two materials.

Here, we applied a reactive-group guided strategy to synthesize dual-structured single-atom nickel sites on RP for photocatalytic water splitting. Single-atom Ni sites were composed of two effective components: P–Ni sites for the reductive reaction and P–O–Ni for the oxidative reaction. This Ni-based catalyst has two different compositions and functionalities, which can be denoted as a Janus structure.[12] Forming these two opposing single-atom active sites achieved simultaneously reduced charge carrier recombination and enhanced surface reactivity, which resulted in improved hydrogen evolution from pure water.

Results and Discussion

The reactive-group guided deposition of Ni single-atom species on red phosphorus (RP) is illustrated in Figure 1a. P–H and P–OH groups are introduced on the surface of RP via a hydrothermal treatment of RP. Then, the hydrothermally treated RP (HRP) is dispersed into a methanol aqueous solution with Ni^{2+} ions. Under light irradiation, photoelectrons and holes are excited in HRP. Ni^{2+} ions around P–H groups capture the activated photoelectrons to form $Ni^{\delta+}$ ($\delta<2$) states and simultaneously substitute H to generate P–Ni bonds, which also prevents $Ni^{\delta+}$ from being further reduced to neutral Ni^0. The remaining holes oxidize CH_3OH in the solution. For the P–OH groups, H is easily ionized into the solution. Ni^{2+} ions can bond with the remaining P–O– to form P–O–Ni, while the holes can be introduced to oxidize the oxygen-bound nickel into $Ni^{\varepsilon+}$ ($\varepsilon>2$) in P–O–Ni. The photoelectrons are consumed by H^+ in water. These reactions were confirmed by XPS studies shown below. Owing to the limited reaction sites and reaction conditions at each reactive group, single-atom Ni sites, rather than Ni nanoparticles, were preferentially generated.

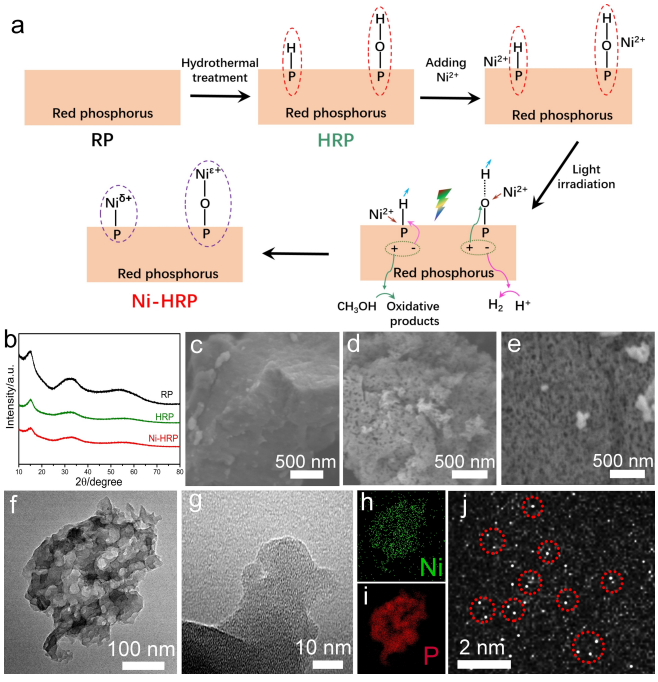

Figure 1. a) Illustration of reactive-group guided synthesis of Ni-HRP. b) XRD patterns of RP, HRP, and Ni-HRP. SEM images of c) RP, d) HRP, and e) Ni-HRP. f) TEM and g) HRTEM images of Ni-HRP. Elemental mapping images for h) Ni and i) P in Ni-HRP. j) HAADF-STEM image of Ni-HRP. The bright spots in the red circles are assigned to single-atom Ni sites.

The broad X-ray powder diffraction (XRD) peaks of RP, HRP, and Ni-HRP indicated their amorphous structures (Figure 1b). No Ni peaks were observed in the XRD pattern of Ni-HRP for its single-atom deposition and low loading amount, which was determined to be 0.92 wt % according to the X-ray fluorescence (XRF) analysis. Scanning electron microscopy (SEM) and transmission electron microscopy (TEM) images revealed that the hydrothermal treatment of RP led to a mesoporous structure in HRP and Ni-HRP (Figure 1c–f), which was verified by pore structure and specific surface area analysis by conducting N_2 physisorption experiments (Figure S1 and Table S1). The mesoporous structure would endow abundant P–H and P–OH groups for the generation of single-atom Ni sites. The high-resolution TEM (HRTEM) and the selected area electron diffraction (SAED) analysis further proved the amorphous structures of RP, HRP, and Ni-HRP (Figure 1g and S2), and the corresponding elemental mapping images confirmed that Ni species were uniformly dispersed in Ni-HRP (Figure 1h,i). The high-angle annular dark-field scanning transmission electron microscopy (HAADF-STEM) images acquired by the spherical aberration-corrected TEM demonstrated the successful formation of well-dispersed single-atom Ni sites in Ni-HRP (Figure 1j and S3), and no Ni-based nanoparticles or clusters were found in agreement with XRD data above. In contrast, as a control experiment, Ni–RP was prepared by directly depositing Ni precursor on commercial RP without a prior hydrothermal treatment. Nickel nanoparticles with an average diameter of 6 nm were observed in Ni–RP (Figure S4), and the measured lattice spacing of 0.202 nm corresponded to metallic Ni.[13]

To confirm the functional groups on the surface of the prepared samples, Fourier transform infrared (FTIR) and ^{31}P solid-state nuclear magnetic resonance (NMR) spectroscopy was applied. As seen in Figure 2a, the peaks at 1632 and 1590 cm^{-1} of all samples belong to the variable vibration of absorbed water. The peaks at 1385 and 1351 cm^{-1} were attributed to the absorbed CO_2 in the air.[14] The peak of RP located at 1103 cm^{-1} was derived from P=O vibration due to the surface oxidation and it disappeared for HRP and Ni-HRP, proving the effective deoxidizing process during the hydrothermal treatment. The peak at 2420 cm^{-1} was indexed to the P–H stretching vibration, confirming the successful generation of P–H groups in HRP.[14c] By comparison with the spectrum of H_3PO_4, the P=O stretching vibration (1150 cm^{-1}), P-$(OH)_3$ antisymmetric stretching vibration (997 cm^{-1}), and P-$(OH)_3$ symmetric stretching vibration (881 cm^{-1}) were confirmed in HRP.[14c] The Ni-HRP catalyst showed the same peaks as HRP, indicating the surface bonding pattern in HRP was retained after depositing the Ni

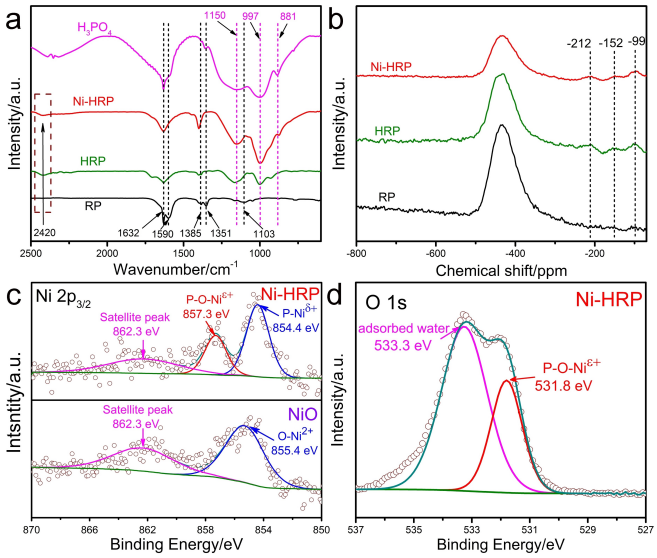

Figure 2. a) FTIR spectra and b) ^{31}P solid-state NMR spectra of the prepared samples. XPS spectra of Ni-HRP for c) Ni 2p (with a NiO reference) and d) O 1s.

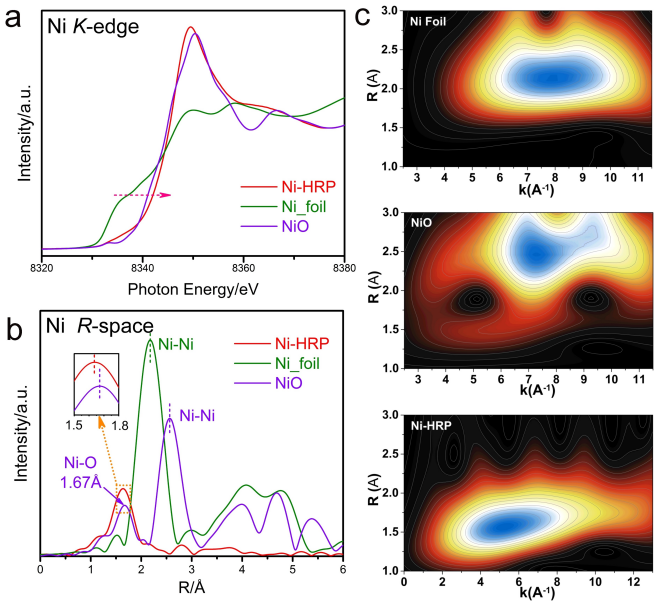

Figure 3. a) Ni K-edge XANES, b) FT-EXAFS spectra, and c) topographical maps of WT-EXAFS of Ni-HRP including references Ni foil and NiO.

species. The ^{31}P solid-state NMR spectra exhibited resonance at about −433 ppm, which were derived from the P–P bond (Figure 2b). The additional peaks of HRP and Ni-HRP at −99, −152, and −212 ppm could be indexed to the P–H bond.[15] No P–OH peaks were detected because NaH_2PO_4 was the reference sample. The FTIR and ^{31}P solid-state NMR results verified that P–H and P–OH groups could be produced on the surface of red phosphorus during the hydrothermal process, and the surface bonds to red phosphorus were kept during the formation of Ni-HRP.

X-ray photoelectron spectroscopy (XPS) analysis was conducted to identify the surface chemical composition. For Ni-HRP, two main peaks of Ni $2p_{3/2}$ centered at 854.4 and 857.3 eV were ascribed to $Ni^{\delta+}$ $(0<\delta<2)$ of P–Ni[16] and $Ni^{\varepsilon+}$ $(\varepsilon>2)$ of P–O–Ni,[17] respectively (Figure 2c). The peak of reference Ni^{2+} in NiO was measured to be 855.4 eV, which was between 854.4 and 857.3 eV, further demonstrating two distinct oxidation states of Ni obtained in Ni-HRP.[6b,16a] The peak located at 862.3 eV belongs to the satellite peak of nickel.[17a] No Ni^0 peak (853.2 eV) could be observed in the spectrum of Ni-HRP.[6b,17c] The O 1s spectra of Ni-HRP displayed two peaks resulting from P–O–Ni at 531.8 eV and adsorbed water at 533.3 eV (Figure 2d).[10a,18] The absence of lattice oxygen signals at 529.5 eV indicated that NiO was not produced in Ni-HRP.[10a,18] The P 2p spectrum of Ni-HRP displayed the typical peaks of red phosphorus (Figure S5). It is difficult to find the P peaks attributed to P–Ni and P–O–Ni, probably due to the much lower abundance compared to the elemental P^0.

X-ray absorption near-edge structure (XANES) and extended X-ray absorption fine structure (EXAFS) spectra were further carried out to verify the possible bonding forms of nickel in Ni-HRP. As shown in Figure 3a, the XANES profiles of Ni K-edge followed the order of Ni-HRP > NiO > Ni foil, which demonstrated that the average valence state of Ni species in Ni-HRP was higher than Ni^{2+}.[19] The coordination environment of Ni was examined by the Fourier-transformed EXAFS (FT-EXAFS) spectra (Figure 3b). It is evident that the notable peak at 1.63 Å was observed and no apparent Ni–Ni peak occurred, indicating that the single-atom Ni site was produced in the sample. The average peak position of Ni-HRP (1.63 Å) was smaller than that of Ni–O (1.67 Å) in the NiO reference sample. We noticed that there were two kinds of bonds (P–Ni bond and P–O–Ni bond) in the XPS spectra. According to the previous report, the P–Ni bond was longer than the Ni–O bond in NiO.[20] The Ni–O bond in P–O–Ni was shorter than the Ni–O bond in NiO.[21] The synergistic effects of P–Ni and P–O–Ni bonds in Ni-HRP led to a slight peak shift compared to the reference NiO. EXAFS wavelet transform (WT) analysis was applied to confirm the atomic dispersion (Figure 3c). The intensity maximum (5.22 Å^{-1}, 1.63 Å) in the topographical map of Ni-HRP was different from those of Ni foil and NiO, further supporting the notion of single-atomic Ni in the sample.

The optical features of the prepared samples were analyzed by Ultraviolet-visible-near infrared diffuse reflectance spectroscopy (UV/Vis-NIR DRS). Loading Ni species increased the visible-infrared light absorption (Figure 4a). The optical band gap values (E_g) of RP, HRP, Ni–RP, and Ni-HRP were calculated to be 1.92, 2.08, 1.86, and 1.98 eV according to the Tauc plots (Figure 4b). The hydrothermal treatment led to a slightly larger band gap of red phosphorus, and loading Ni-based cocatalysts could decrease the band gap. The flat band potentials of all samples could be obtained from the Mott–Schottky plots (Figure 4c). Generally, the conduction band (CB) edge can be considered to be about 0.1 V negative of the flat band potential for the n-type semiconductor.[22] Therefore, the CB positions of

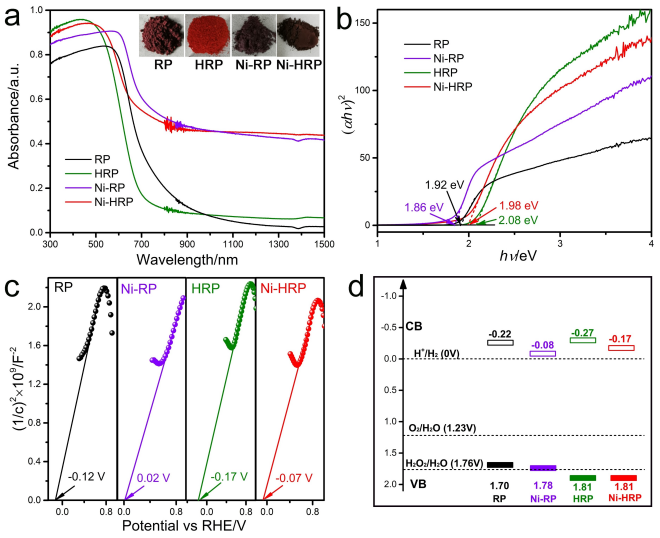

Figure 4. a) UV/Vis-NIR DRS spectra of prepared samples. Insets are the digital photographs of the photocatalyst powders. b) Tauc plots, c) Mott–Schottky plots, and d) band structure illustration of all samples.

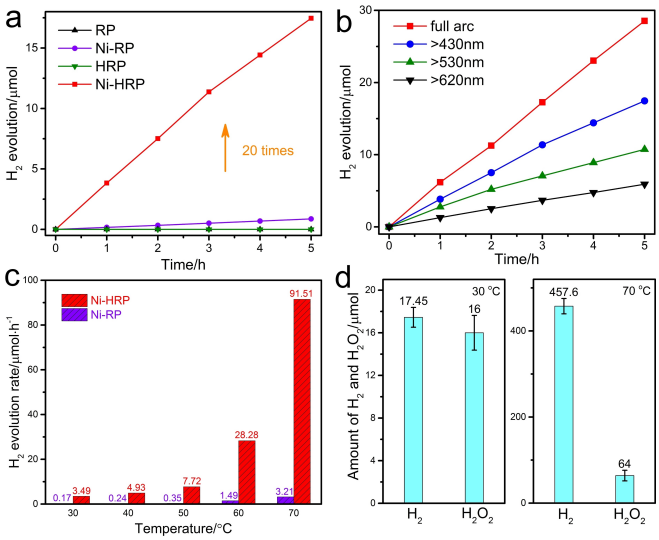

Figure 5. a) H_2 evolution tests of prepared samples under visible light irradiation ($\lambda > 430$ nm) at 30 °C. b) H_2 evolution tests of Ni-HRP under incident light with varied wavelengths at 30 °C. c) 5 h average H_2 evolution rates of Ni–RP and Ni-HRP at different temperatures under visible light irradiation. d) The actual amount of evolved H_2 and H_2O_2 after a 5 h photocatalytic reaction at 30 °C and 70 °C under visible light irradiation.

HRP and Ni-HRP were determined. Correspondingly, the band structures of HRP and Ni-HRP are illustrated (Figure 4d). According to the energy band analysis, it is found that the CB and VB positions of HRP and Ni-HRP fulfill the requirements for water splitting.

The photocatalytic activity for hydrogen production was investigated in pure water without using any sacrificial reagent. The bare RP and HRP didn't show apparent hydrogen production (Figure 5a), while Ni-HRP showed remarkable hydrogen production with optimized photodeposition time of Ni species (Figure S6). The added amount of Ni precursor to prepare Ni-HRP was varied, and the hydrogen production rate didn't change significantly when the used Ni precursor amount exceeded 60 mg (Figure S7). Impressively, the Ni-HRP photocatalysts with Ni single-atom sites presented a 20 times higher activity than the Ni–RP photocatalysts with 6-nm Ni nanoparticles deposited on the RP (Figure S4). Furthermore, Ni-HRP exhibited photocatalytic hydrogen production under long-wave light irradiation ($\lambda > 620$ nm, Figure 5b), confirming its wide-spectrum light response for photocatalysis. Because the light absorption of Ni-HRP above 800 nm was much stronger than that of HRP, the photocatalytic hydrogen production of Ni-HRP was also tested under light irradiation with $\lambda > 800$ nm. However, there was no apparent hydrogen production. Thus, while light absorption above 800 nm can be attributed to the Ni addition to the catalyst, the 800 nm-photogenerated excitations do not have enough driving force for efficient water splitting.

During the photocatalytic tests, light not only provides photons for the chemical reaction but also heats the reaction system. Thus, the thermal-assisted photocatalytic activity was also studied by varying the reaction temperature. Impressively, Ni-HRP exhibited boosted activity with increased reaction temperature, reaching an activity of 91.51 μmol h^{-1} at 70 °C (Figure 5c). The corresponding apparent quantum efficiency (AQE) for hydrogen production reached 8.9 % at 420 nm, which is better than most previous reports using non-metal phosphorus or carbon nitride-based photocatalysts (Table S2 for a literature comparison). Although the increased reaction temperature could enhance the photocatalytic activity of Ni–RP, the hydrogen production rate was still quite low. RP and HRP didn't show apparent H_2 evolution even at 70 °C. The activation energies for hydrogen evolution over Ni–RP and Ni-HRP were calculated to be 65.98 and 70.86 kJ mol^{-1}, respectively (Figure S8). To test the stability of Ni-HRP, a 48 h photocatalytic test at 30 °C and a 16-h test at 70 °C were measured. The photocatalyst showed good stability at 30 °C (Figure S9a), but the stability at 70 °C was poor (Figure S9b). The XRD, XPS, and TEM analysis of Ni-HRP before and after the photocatalytic reaction was performed (Figure S10–S12). It was found that the amorphous structure, surface composition, and elemental valence states were not changed after the photocatalytic reactions at 30 °C and 70 °C. The morphology of Ni-HRP was unchanged after the reaction at 30 °C, but the large Ni-HRP sheets were broken into small pieces after the reaction at 70 °C.

Note that no O_2 was detected during the water-splitting reaction. It has been reported that H_2O_2 was the oxidative product for phosphorus and some phosphorus-coated catalysts.[8b,c] The electron transfer number (n) was determined to be 2.08 via the rotating ring-disk electrode (RRDE) collection experiment (Figure S13), which confirmed that H_2O_2 was generated through a 2e$^-$-pathway.[23] Electrochemical tests using the reaction solution as the electrolyte showed the apparent current attributed to the

generation of H_2O_2 (Figure S14). After MnO_2 was added, H_2O_2 was decomposed, resulting in a significantly decreased current.[8b] The amount of produced H_2O_2 can be determined by a titration experiment.[24] When the reaction temperature was 30 °C, the molar ratio of generated H_2 to H_2O_2 was close to 1:1. However, the amount of produced H_2O_2 was deficient compared to the amount of H_2, when the reaction temperature reached 70 °C (Figure 5d). Through the TEM results of Ni-HRP before and after the photocatalytic reaction (Figure S12), it was found that the large Ni-HRP sheets were broken into small pieces. Therefore, it was inferred that the deficient H_2O_2 amount at 70 °C could be ascribed to the corrosion reaction of HRP with H_2O_2, according to Equation (1).

$$2P + 5H_2O_2 \rightarrow 2H_3PO_4 + 2H_2O \quad (1)$$

The Gibbs free energy change of this chemical reaction was calculated to be negative, which confirmed that (1) is a spontaneous reaction (for detailed calculations see Supporting Information). To prove the hypothesis, 40 mg of HRP or Ni-HRP was dispersed into 80 mL of aqueous solution with 10 mmol of H_2O_2. After stirring for 5 h, the solution became transparent (Figure S15), which indicated that RP-based materials reacted with H_2O_2. Comparative experiments also revealed that H_2O_2 could corrode Ni-HRP (Figures S16 and S17), but no H_2 was detected during the corrosion process. It should be noted that the concentration of produced H_2O_2 during the photocatalytic reaction was much lower. When the molar ratio of generated H_2O_2 to H_2 was equal to 1:1, the amounts of H_2O_2 after a 5 h photocatalytic reaction at 30 and 70 °C should be only 17.45 and 457.6 μmol, respectively, in 80 mL of the reaction solution. To simulate the corrosion process during the photocatalytic reaction, 40 mg of Ni-HRP were dispersed into 80 mL of aqueous solution with 20 or 500 μmol of H_2O_2 to form suspension A or suspension B, respectively. After stirring for 24 h, the color of suspension A didn't change, but the color of suspension B became much lighter (Figure S18). This phenomenon indicated that the corrosion of Ni-HRP was dependent on the H_2O_2 concentration, which could explain the good stability and close molar amounts of H_2 and H_2O_2 during the photocatalytic reaction at 30 °C. In contrast, the photocatalytic stability was poor at 70 °C, and the amount of H_2O_2 was seriously deficient compared to that of H_2. However, the corrosion process could not be fully avoided when the photocatalytic reaction took place at 30 °C. This is why the measured H_2O_2 amount was slightly lower than the H_2 amount at 30 °C (Figure 5d). This result could also explain the unstable cyclic H_2 production in some previous reports about RP photocatalysts.[25] A potential way to improve the stability can be using a fixed-bed reactor combined with a flowing reaction solution to decrease the exposure time of photocatalysts to the produced H_2O_2.

To explain the superior photocatalytic activity of Ni-HRP, the charge transfer properties of the prepared samples were determined. The steady-state photoluminescence (PL) spectra and the surface photovoltage (SPV) spectra were measured. Loading Ni-based cocatalysts decreased the PL signals of HRP and RP. The stronger quenching effect in Ni-HRP compared to that in Ni–RP indicated the role of the Ni single-atom sites in suppressing the radiative electron-hole recombination (Figure 6a).[26] The increased surface photovoltage (SPV) intensity of Ni-HRP confirmed the efficient separation of photogenerated electron-hole pairs (Figure 6b),[27] which was further supported by the electrochemical impedance spectroscopy (EIS) analysis (Figure 6c and Table S3). The linear sweep voltammetry (LSV) curves demonstrated better catalytic properties of Ni-HRP for both water reduction and oxidation (Figure 6d).[11]

To uncover the mechanism of the HER and the hydrogen peroxide evolution reaction (HPER) process, DFT-based calculations were carried out. Figure 7a shows the geometric structure of red phosphorous with P–Ni and P–O–Ni sites and the corresponding *H adsorption geometries. Although red phosphorous appears as an amorphous phase, it has been widely accepted that its structure is based on tubular components of five- or six-membered rings with covalent bonds between the P atoms.[8d] We, therefore, selected the type IV triclinic fibrous RP (001) surface as the model for theoretical calculations. At both P–Ni and P–O–Ni sites, Ni was 4-fold coordinated, which provides stable adsorption configurations (Figure S19). As shown in Figure 7b, the P–Ni site ($\Delta G_{*H} = 0.13$ eV) exhibits better HER activity than the P–O–Ni site ($\Delta G_{*H} = 1.00$ eV), since the free energy of *H (the star signifies that the hydrogen is adsorbed) at the P–Ni site is closer to the optimal value ($|\Delta G_{*H}| \cong 0$ eV).[28] Very recent work also corroborates that P–Ni could serve as an excellent site for the HER process.[29] On the other hand, the HPER process could be subdivided into three steps in neutral media (see Supporting Information). As a result of adsorbed *OH stabilization, the third

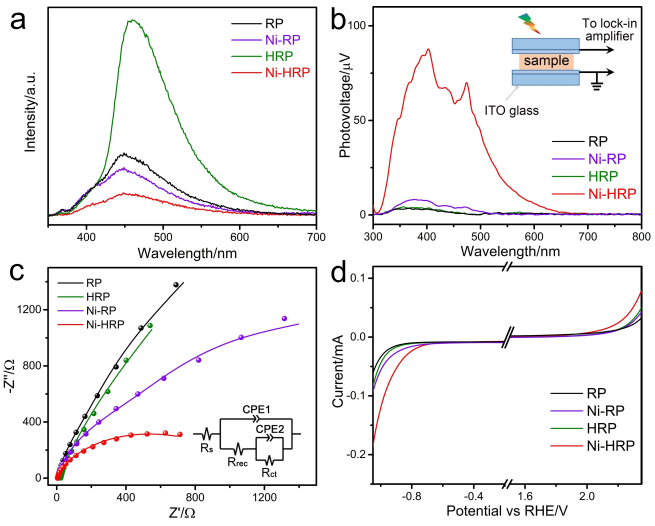

Figure 6. a) Steady-state photoluminescence (PL) spectra of all samples with an excitation wavelength of 337 nm. b) Surface photovoltage (SPV) spectra of HRP and Ni-HRP with a 500 W Xe lamp as the light source, and the inset is the schematic setup for the SPV measurement. c) Nyquist plots of HRP and Ni-HRP in 0.5 M Na_2SO_4 aqueous solution. The inset is the equivalent circuit. d) Linear sweep voltammetry (LSV) curves of the different samples.

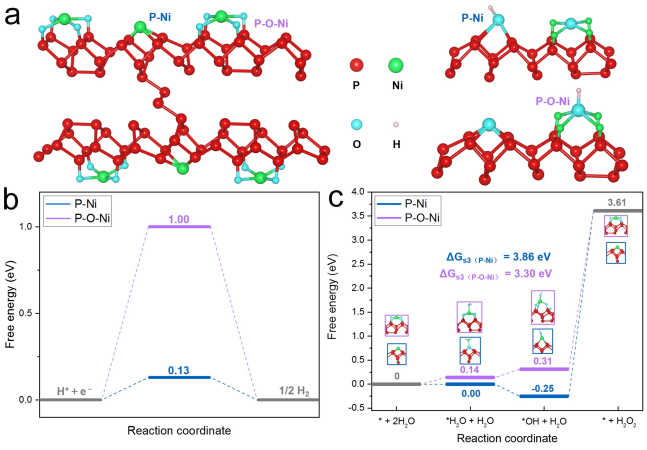

Figure 7. a) Geometric structures of red phosphorus with P–Ni and P–O–Ni sites and the corresponding hydrogen adsorption geometries. b) DFT calculation of free energy of H adsorption (ΔG_{*H}) at P–Ni (blue) and P–O–Ni (purple) sites. c) Free energy diagram for the three-step HPER process on P–Ni (blue) and P–O–Ni (purple) sites. The star (*) represents the catalytic adsorption site.

step, namely from *OH to *H_2O_2, is thermodynamically the most difficult for the entire process, as shown in Figure 7c. The P–O–Ni site ($\Delta G_{s3(P-O-Ni)} = 3.30$ eV) shows a lower free energy barrier for HPER than the P–Ni site ($\Delta G_{s3(P-Ni)} = 3.86$ eV), suggesting that the HPER process is more likely to occur at the P–O–Ni site. As a consequence, the DFT-based calculations indicate that the P–Ni site prefers to be an active site for water reduction to hydrogen while the P–O–Ni site for water oxidation to H_2O_2.

Through the reactive-group guided synthesis, single-atom Ni species were dispersed on the hydrothermally treated red phosphorus (HRP) in the forms of P–Ni and P–O–Ni, which function as redox-active sites for water splitting. The catalytic functions have been verified by the LSV results (Figure 6d). According to the band structure analysis (Figure 4d), it is plausible that Ni-HRP can generate H_2 and H_2O_2 simultaneously. The photogenerated electrons will transfer to P–Ni sites and reduce water to H_2, while the holes migrate to P–O–Ni sites and oxidize water to H_2O_2 (Figure S20). The catalytic roles of P–Ni and P–O–Ni groups were also demonstrated in previous reports.[9,10] Benefitting from this Ni-based Janus structure, effective charge separation, as well as accelerated surface reactivity can be obtained, as verified by the PL, SPV, EIS, LSV, and computational results. Upon the deposition of the Ni-cocatalyst on HRP and RP, the conduction band positions were slightly lowered (Figure 4d) and the catalytic activity was improved in both types of materials (Figure 5a). Strongly elevated hydrogen evolution from water splitting was achieved with Ni-HRP.

Conclusion

In summary, a reactive-group guided strategy was adopted to fabricate nickel-based single-atom sites over red phosphorus photocatalyst. The P–H and P–OH surface groups generated during the hydrothermal process are the templates according to which the subsequent formation of P–Ni and P–O–Ni structures are controlled during the photodeposition step. These two chemical functionalities, considered together, form a Janus structure working together on complementary tasks: P–Ni on water reduction and P–O–Ni on water oxidation, leading to the efficient separation of electron-hole pairs and overall improved photocatalytic water splitting activity. The photocatalyst exhibited excellent hydrogen evolution from pure water, especially at elevated temperatures. This work not only presents a high-efficiency photocatalyst but also provides a new strategy to design advanced single-atom dual-function catalysts for overall water splitting. In addition, the insightful analysis of the stability can provide useful guidance to design durable red phosphorus-based photocatalysts in the future.

Acknowledgements

The authors thank for the support from the National Natural Science Foundation of China (Nos. 51888103, 52076177), China National Key Research and Development Plan Project (No. 2021YFF0500503), Shaanxi Technical Innovation Guidance Project (No. 2018HJCG-14), Sichuan Science and Technology Program (No. 2021YFSY0047), the Natural Science Basic Research Program of Shaanxi Province (2019JCW-10), and China Fundamental Research Funds for the Central Universities.

Conflict of Interest

The authors declare no conflict of interest.

Data Availability Statement

The data that support the findings of this study are available in the Supporting Information of this article.

Keywords: Nickel · Photocatalysis · Red Phosphorus · Single-Atom Catalysts · Water Splitting

[1] a) A. Kudo, Y. Miseki, *Chem. Soc. Rev.* **2009**, *38*, 253–278; b) S. Wang, G. Liu, L. Wang, *Chem. Rev.* **2019**, *119*, 5192–5247; c) S. Chen, T. Takata, K. Domen, *Nat. Rev. Mater.* **2017**, *2*, 17050.

[2] a) R. Daghrir, P. Drogui, D. Robert, *Ind. Eng. Chem. Res.* **2013**, *52*, 3581–3599; b) X. Wang, S. Blechert, M. Antonietti, *ACS Catal.* **2012**, *2*, 1596–1606; c) K. Zhang, L. Guo, *Catal. Sci. Technol.* **2013**, *3*, 1672–1690; d) Y. Chen, X. Feng, Y. Liu, X. Guan, C. Burda, L. Guo, *ACS Energy Lett.* **2020**, *5*, 844–866.

[3] a) J. Ran, J. Zhang, H. Yu, M. Jaroniec, S. Qiao, *Chem. Soc. Rev.* **2014**, *43*, 7787; b) Z. Qin, Y. Chen, X. Wang, X. Guo, L. Guo, *ACS Appl. Mater. Interfaces* **2016**, *8*, 1264–1272; c) C. Cheng, S. Zong, J. Shi, F. Xue, Y. Zhang, X. Guan, B. Zheng, J. Deng, L. Guo, *Appl. Catal. B* **2020**, *265*, 118620.

[4] a) B. Wang, H. Cai, S. Shen, *Small Methods* **2019**, *3*, 1800447; b) C. Gao, J. Low, R. Long, T. Kong, J. Zhu, Y. Xiong, *Chem. Rev.* **2020**, *120*, 12175–12216.
[5] a) X. Li, W. Bi, L. Zhang, S. Tao, W. Chu, Q. Zhang, Y. Luo, C. Wu, Y. Xie, *Adv. Mater.* **2016**, *28*, 2427–2431; b) G. Gao, Y. Jiao, E. R. Waclawik, A. Du, *J. Am. Chem. Soc.* **2016**, *138*, 6292–6297; c) Z. Geng, Y. Liu, X. Kong, P. Li, K. Li, Z. Liu, J. Du, M. Shu, R. Si, J. Zeng, *Adv. Mater.* **2018**, *30*, 1803498.
[6] a) X. Jin, R. Wang, L. Zhang, R. Si, M. Shen, M. Wang, J. Tian, J. Shi, *Angew. Chem. Int. Ed.* **2020**, *59*, 6827–6831; *Angew. Chem.* **2020**, *132*, 6894–6898; b) Y. Li, Y. Wang, C. L. Dong, Y. C. Huang, J. Chen, Z. Zhang, F. Meng, Q. Zhang, Y. Huangfu, D. Zhao, L. Gu, S. Shen, *Chem. Sci.* **2021**, *12*, 3633.
[7] a) M. Zhu, S. Kim, L. Mao, M. Fujitsuka, J. Zhang, X. Wang, T. Majima, *J. Am. Chem. Soc.* **2017**, *139*, 13234–13242; b) Z. Zhang, J. Huang, Y. Fang, M. Zhang, K. Liu, B. Dong, *Adv. Mater.* **2017**, *29*, 1606688.
[8] a) Z. Hu, Z. Shen, J. C. Yu, *Green Chem.* **2017**, *19*, 588–613; b) M. Wang, Z. Qin, Z. Diao, R. Li, J. Zhong, D. Ma, Y. Chen, *ACS Sustainable Chem. Eng.* **2020**, *8*, 13459–13466; c) Y. Zhu, C. Lv, Z. Yin, J. Ren, X. Yang, C. Dong, H. Liu, R. Cai, Y. C. Huang, W. Theis, S. Shen, D. Yang, *Angew. Chem. Int. Ed.* **2020**, *59*, 868–873; *Angew. Chem.* **2020**, *132*, 878–883; d) C. M. Fung, C. C. Er, L. L. Tan, A. M. Mohamed, S. P. Chai, *Chem. Rev.* **2022**, *122*, 3879–3965; e) F. Wang, W. K. H. Ng, J. C. Yu, H. Zhu, C. Li, L. Zhang, Z. Liu, Q. Li, *Appl. Catal. B* **2012**, *111–112*, 409–414.
[9] a) Y. Chen, Z. Qin, *Catal. Sci. Technol.* **2016**, *6*, 8212; b) Z. Qin, F. Xue, Y. Chen, S. Shen, L. Guo, *Appl. Catal. B* **2017**, *217*, 551–559.
[10] a) Y. Li, C. Zhao, *Chem. Mater.* **2016**, *28*, 5659–5666; b) M. Barroso, A. J. Cowan, S. R. Pendlebury, M. Grätzel, D. R. Klug, J. R. Durrant, *J. Am. Chem. Soc.* **2011**, *133*, 14868–14871.
[11] Z. Qin, Y. Chen, Z. Huang, J. Su, L. Guo, *J. Mater. Chem. A* **2017**, *5*, 19025.
[12] a) L. A. Stern, L. Feng, F. Song, X. Hu, *Energy Environ. Sci.* **2015**, *8*, 2347; b) S. Cobo, J. Heidkamp, P. A. Jacques, J. Fize, V. Fourmond, L. Guetaz, B. Jousselme, V. Ivanova, H. Dau, S. Palacin, M. Fontecave, V. Artero, *Nat. Mater.* **2012**, *11*, 802–807; c) J. Yang, J. Wang, Y. Liu, H. Li, Z. Lin, *Mater. Horiz.* **2020**, *7*, 3242.
[13] a) L. Kong, Y. Dong, P. Jiang, G. Wang, H. Zhang, N. Zhao, *J. Mater. Chem. A* **2016**, *4*, 9998; b) C. Sun, H. Zhang, H. Liu, X. Zheng, W. Zou, L. Dong, L. Qi, *Appl. Catal. B* **2018**, *235*, 66–74.
[14] a) K. Coenen, F. Gallucci, B. Mezari, E. Hensen, M. S. Annaland, *J. CO2 Util.* **2018**, *24*, 228–239; b) W. R. Stevens, Jr., R. V. Siriwardane, J. Logan, *Energy Fuels* **2008**, *22*, 3070–3079; c) J. A. Dean, *LANGE'S Handbook of Chemistry 15th ed.*, McGraw-Hill, New York, **1999**.
[15] O. Kühl, *Phosphorus-31 NMR Spectroscopy: A Concise Introduction for the Synthetic Organic and Organometallic Chemist*, Springer, Heidelberg, **2008**.
[16] a) J. Shi, Y. Zou, L. Cheng, D. Ma, D. Sun, S. Mao, L. Sun, C. He, Z. Wang, *Chem. Eng. J.* **2019**, *378*, 122161; b) H. Yang, Q. Lin, C. Zhang, X. Yu, Z. Cheng, G. Li, Q. Hu, X. Ren, Q. Zhang, J. Liu, C. He, *Nat. Commun.* **2020**, *11*, 593.
[17] a) Z. Xiao, Y. Bao, Z. Li, X. Huai, M. Wang, P. Liu, L. Wang, *ACS Appl. Energy Mater.* **2019**, *2*, 1086–1092; b) F. S. Omar, A. Numan, S. Bashir, N. Duraisamy, R. Vikneswaran, Y. L. Loo, K. Ramesh, S. Ramesh, *Electrochim. Acta* **2018**, *273*, 216–228; c) Y. N. Gong, L. Jiao, Y. Qian, C. Y. Pan, L. Zheng, X. Cai, B. Liu, S. H. Yu, H. L. Jiang, *Angew. Chem. Int. Ed.* **2020**, *59*, 2705–2709; *Angew. Chem.* **2020**, *132*, 2727–2731.
[18] M. A. Peck, M. A. Langell, *Chem. Mater.* **2012**, *24*, 4483–4490.
[19] a) W. Zheng, F. Chen, Q. Zeng, Z. Li, B. Yang, L. Lei, Q. Zhang, F. He, X. Wu, Y. Hou, *Nano-Micro Lett.* **2020**, *12*, 108; b) Y. Li, Z. S. Wu, P. Lu, X. Wang, W. Liu, Z. Liu, J. Ma, W. Ren, Z. Jiang, X. Bao, *Adv. Sci.* **2020**, *7*, 1903089.
[20] a) S. T. Oyama, X. Wang, Y.-K. Lee, K. Bando, F. G. Requejo, *J. Catal.* **2002**, *210*, 207–217; b) J. Song, Z. Wei, Z. Pan, Z. Xie, S. Wei, *AIP Conf. Proc.* **2007**, *882*, 453; c) W. Liu, L. Cao, W. Cheng, Y. Cao, X. Liu, W. Zhang, X. Mou, L. Jin, X. Zheng, W. Che, Q. Liu, T. Yao, S. Wei, *Angew. Chem. Int. Ed.* **2017**, *56*, 9312–9317; *Angew. Chem.* **2017**, *129*, 9440–9445.
[21] G. Berhault, P. Afanasiev, H. Loboué, C. Geantet, T. Cseri, C. Pichon, C. Guilliot-Deudon, A. Lafond, *Inorg. Chem.* **2009**, *48*, 2985–2992.
[22] a) H. Wakayama, K. Utimula, T. Ichibha, R. Kuriki, K. Hongo, R. Maezono, K. Oka, K. Maeda, *J. Phys. Chem. C* **2018**, *122*, 26506–26511; b) B. Dong, J. Cui, T. Liu, Y. Gao, Y. Qi, D. Li, F. Xiong, F. Zhang, C. Li, *Adv. Energy Mater.* **2018**, *8*, 1801660.
[23] a) D. Wei, Y. Tan, Y. Wang, T. Kong, S. Shen, S. S. Mao, *Sci. Bull.* **2020**, *65*, 1389–1395; b) F. Xue, Y. Si, M. Wang, M. Liu, L. Guo, *Nano Energy* **2019**, *62*, 823–831.
[24] T. M. Gill, X. Zheng, *Chem. Mater.* **2020**, *32*, 6285–6294.
[25] R. Shi, F. Liu, Z. Wang, Y. Weng, Y. Chen, *Chem. Commun.* **2019**, *55*, 12531.
[26] X. Guo, P. Guo, C. Wang, Y. Chen, L. Guo, *Chem. Eng. J.* **2020**, *383*, 123183.
[27] a) D. Zhao, C. L. Dong, B. Wang, C. Chen, Y. C. Huang, Z. Diao, S. Li, L. Guo, S. Shen, *Adv. Mater.* **2019**, *31*, 1903545; b) D. Zhao, Y. Wang, C. L. Dong, Y. C. Huang, J. Chen, F. Xue, S. Shen, L. Guo, *Nat. Energy* **2021**, *6*, 388–397.
[28] J. K. Nørskov, T. Bligaard, A. Logadottir A, J. R. Kitchin, J. G. Chen, S. Pandelov, U. Stimming, *J. Electrochem. Soc.* **2005**, *152*, J23–J26.
[29] Z. Qian, L. Liao, Q. Bian, F. Yu, D. Li, J. Zeng, L. Zhang, H. Wang, D. Tang, H. Zhou, Z. Ren, *Small* **2022**, *18*, 2105642.

Manuscript received: March 30, 2022
Accepted manuscript online: May 6, 2022
Version of record online: May 25, 2022